Title

aE-catenin actin-binding domain alters actin filament conformation and regulates binding of nucleation and disassembly factors.

Journal

Molecular biology of the cell, 24(23)

Authors

Mullins, RD
Hansen, SD
Kwiatkowski, AV
et al.

Publication Date

2013-09-25

Peer reviewed

αE-catenin actin-binding domain alters actin filament conformation and regulates binding of nucleation and disassembly factors

Scott D. Hansen[a,*], Adam V. Kwiatkowski[b,c,*], Chung-Yueh Ouyang[d], HongJun Liu[d], Sabine Pokutta[e], Simon C. Watkins[c], Niels Volkmann[d], Dorit Hanein[d], William I. Weis[e,f], R. Dyche Mullins[a], and W. James Nelson[b,f]

[a]Department of Cellular and Molecular Pharmacology, University of California, San Francisco, School of Medicine, San Francisco, CA 94158; [b]Department of Biology, Stanford University, Stanford, CA 94305; [c]Department of Cell Biology, University of Pittsburgh School of Medicine, Pittsburgh, PA 15261; [d]Bioinformatics and Systems Biology Program, Sanford Burnham Medical Research Institute, La Jolla, CA 92037; [e]Department of Structural Biology and [f]Department of Molecular and Cellular Physiology, Stanford University School of Medicine, Stanford, CA 94305

ABSTRACT **The actin-binding protein αE-catenin may contribute to transitions between cell migration and cell–cell adhesion that depend on remodeling the actin cytoskeleton, but the underlying mechanisms are unknown. We show that the αE-catenin actin-binding domain (ABD) binds cooperatively to individual actin filaments and that binding is accompanied by a conformational change in the actin protomer that affects filament structure. αE-catenin ABD binding limits barbed-end growth, especially in actin filament bundles. αE-catenin ABD inhibits actin filament branching by the Arp2/3 complex and severing by cofilin, both of which contact regions of the actin protomer that are structurally altered by αE-catenin ABD binding. In epithelial cells, there is little correlation between the distribution of αE-catenin and the Arp2/3 complex at developing cell–cell contacts. Our results indicate that αE-catenin binding to filamentous actin favors assembly of unbranched filament bundles that are protected from severing over more dynamic, branched filament arrays.**

Monitoring Editor
Alpha Yap
University of Queensland

Received: Jul 16, 2013
Revised: Sep 3, 2013
Accepted: Sep 19, 2013

INTRODUCTION

The regulation of actin cytoskeleton dynamics and organization is essential for cell migration and cell–cell adhesion during embryonic development and in the adult organism (Halbleib and Nelson, 2006; Ratheesh and Yap, 2012) and is often altered in diseases such as metastatic cancers (Condeelis *et al.*, 2005). The spatial organization of filamentous actin (F-actin) differs between single migrating cells and stationary cells that have strong cell–cell adhesions. In motile cells, dynamic and highly branched actin networks drive membrane protrusion (Svitkina and Borisy, 1999), whereas in adherent cells bundles of unbranched filaments are organized parallel to the plasma membrane to stabilize cell–cell contacts (Hirokawa *et al.*, 1983). How actin-binding proteins coordinate transitions between these distinct actin network architectures and hence cell behaviors is unclear.

A candidate regulator of actin organization is αE-catenin, an actin-binding protein of the cadherin cell–cell adhesion complex (Aberle *et al.*, 1994; Rimm *et al.*, 1995). In mammals, αE-catenin is allosterically regulated: the monomer binds β-catenin/cadherin, whereas the homodimer does not bind β-catenin but interacts with F-actin (Drees *et al.*, 2005). Significantly, selective depletion of the cytoplasmic pool of αE-catenin in mammalian cells does not affect cell–cell adhesion but increases membrane protrusion and accelerates cell migration (Benjamin *et al.*, 2010), indicating that cytoplasmic αE-catenin regulates actin dynamics independently of the cadherin complex. Indeed, deletion of αE-catenin in mice causes defects in not only cell–cell adhesion but also cell migration and proliferation (Vasioukhin *et al.*, 2000), and in humans it coincides

This article was published online ahead of print in MBoC in Press (http://www.molbiolcell.org/cgi/doi/10.1091/mbc.E13-07-0388) on September 25, 2013.

*These authors contributed equally to this work.

Address correspondence to: R. Dyche Mullins (dyche@mullinslab.ucsf.edu), W. James Nelson (wjnelson@stanford.edu).

Abbreviations used: ABD, actin-binding domain; F-actin, filamentous actin; GFP, green fluorescent protein; SIM, structured illumination microscopy.

with metastatic cancers with a worse prognosis than deletion of E-cadherin alone (Benjamin and Nelson, 2008). Together these results indicate that αE-catenin plays multiple roles in cell–cell adhesion and cell migration. However, there is little mechanistic understanding of how αE-catenin regulates different aspects of actin polymerization and organization necessary to effect changes in cell behavior during transitions between migratory cells and more stationary cell aggregates.

αE-catenin is structurally similar to vinculin, another actin-binding protein that links transmembrane proteins to the actin cytoskeleton. Sequence and structural data indicate that αE-catenin and vinculin are organized as a series of four-helix bundles with a five-helix C-terminal "tail" that binds filamentous actin (the actin-binding domain [ABD]; Figure 1A; Bakolitsa *et al.*, 1999, 2004; Pokutta and Weis, 2000; Pokutta *et al.*, 2002; Yang *et al.*, 2001; Borgon *et al.*, 2004; Janssen *et al.*, 2006; Kwiatkowski *et al.*, 2010; Choi *et al.*, 2012; Rangarajan and Izard, 2012; Ishiyama *et al.*, 2013; Miller *et al.*, 2013). Like that of αE-catenin, vinculin activity is conformationally regulated: intramolecular interactions between the vinculin tail and the N-terminal "head" maintain the protein in a closed conformation and inhibit actin filament binding (Johnson and Craig, 1994, 1995). In contrast to mammalian αE-catenin, full-length vinculin is a monomer in solution, and ligand binding relieves autoinhibition (Bakolitsa *et al.*, 1999; Janssen *et al.*, 2006). For example, talin binding to the vinculin head stabilizes a conformation in which the tail ABD can associate with filamentous actin (Izard *et al.*, 2004). A single vinculin ABD contacts portions of two adjacent actin monomers along the long-pitch helix of the filament, and actin filament binding is associated with rearrangements within the vinculin tail that promote dimerization and actin bundle formation (Janssen *et al.*, 2006).

Compared to our molecular understanding of how vinculin binds and organizes actin filaments, many important questions about αE-catenin remain unanswered. Although αE-catenin homodimers bind and bundle actin filaments (Rimm *et al.*, 1995; Drees *et al.*, 2005), it is not known how αE-catenin docks along the filament or whether this interaction affects the conformation of protomers within the actin filament or the assembly and disassembly dynamics of the actin filament. Bulk assays revealed that αE-catenin inhibits actin filament nucleation by the Arp2/3 complex (Drees *et al.*, 2005); however, it is not known whether this is caused by a direct effect on barbed-end elongation, inhibition of Arp2/3 complex branching activity by changes in actin protomer conformation within the filament, or steric inhibition. Finally, actin dynamics is also regulated by severing proteins such as cofilin (Oser and Condeelis, 2009), and it is unknown whether αE-catenin binding to actin filaments affects these activities as well. Answers to these questions would provide a significant advance in defining the functional diversity of αE-catenin.

To address these critical gaps in the understanding of αE-catenin mechanism, we used a combination of cryo–electron microscopy (cryo-EM), total internal reflection fluorescence microscopy (TIRF-M) of reconstituted actin filaments, and superresolution structured illumination microscopy (SIM) in cells to visualize αE-catenin binding to actin filaments and examine αE-catenin–mediated regulation of actin assembly and disassembly with single-filament resolution. Our results provide a mechanistic framework for how αE-catenin regulates actin organization and support a role for αE-catenin in regulating transitions from branched to linear actin networks that accompany switches between cellular migratory and adhesive states.

RESULTS

Mammalian αE-catenin exists as a monomer and homodimer in solution (Rangarajan and Izard, 2013), and the oligomeric state appears to regulate actin filament binding (Drees *et al.*, 2005), perhaps by affecting accessibility of the ABD (Rangarajan and Izard, 2013). The primary filamentous actin-binding region in αE-catenin is located in the C-terminal ABD (amino acids [aa] 671–906), a five-helix bundle with significant homology to the corresponding domain in vinculin (Figure 1A). Therefore, in addition to full-length αE-catenin, we used the monomeric αE-catenin ABD to cleanly dissect the molecular details of actin binding without the complication of potential intramolecular regulation due to the presence of the amino-terminal homodimerization domain (Figure 1A and Supplemental Figure S1A).

Using TIRF-M, we visualized green fluorescent protein (GFP)–tagged αE-catenin ABD binding to phalloidin-stabilized actin filaments in vitro. GFP αE-catenin ABD bound cooperatively to actin filaments with a Hill coefficient of 3.3 and $K_d \approx 0.5$ μM (Figure 1, B and C, and Supplemental Figure S1B), similar to "dark" (unlabeled) αE-catenin ABD measured in bulk actin filament cosedimentation assays (Hill coefficient between 3 and 4; $K_d \approx 1.0$ μM; Supplemental Figure S1C). "Dark" full-length αE-catenin dimer bound actin filaments with a similar affinity, although the binding was less cooperative (Supplemental Figure S1D). Consistent with cooperative binding, we observed a concentration-dependent change in the dwell time of single GFP αE-catenin ABD molecules bound to individual actin filaments (Figure 1, D–G, and Supplemental Movies S1 and S2). When GFP αE-catenin ABD was diluted to 2 nM, the average dwell time for single molecules interacting with filamentous actin was 70 ± 2 ms (Figure 1, D and E). However, when 2 nM GFP αE-catenin ABD was mixed with 0.5 μM dark αE-catenin ABD, we observed two populations of GFP αE-catenin ABD: 1) rapidly dissociating, 88 ± 3 ms (58%), and 2) slowly dissociating, 659 ± 15 ms (42%; Figure 1, D and F). In the presence of 1.0 μM dark αE-catenin ABD, the dwell times for single GFP αE-catenin ABD molecules binding to filamentous actin was further extended to 986 ± 26 ms (36%; slowly dissociating; Figure 1, D and G). The approximately 14-fold increase in the dwell time for GFP αE-catenin ABD in the presence of dark αE-catenin ABD is consistent with cooperative binding.

To understand the αE-catenin-actin filament interaction in molecular detail, we obtained three-dimensional (3D) cryo-EM reconstructions of αE-catenin ABD-actin filament assemblies. Consistent with cooperative binding of αE-catenin ABD to filamentous actin, we observed either bare actin filaments (Figure 2A, filaments marked red) or filaments with bound αE-catenin ABD (Figure 2A, filaments marked blue). Reconstructions of bare actin filaments (Figure 2B) and αE-catenin ABD actin filament assemblies (Figure 2C) were obtained at ~1.8-nm resolution. Aided by difference mapping, we determined that αE-catenin ABD contacts two adjacent actin subunits along the long-pitch helix of the actin filament (Figure 2C, single ABD shaded blue). This binding interface explains why αE-catenin ABD binds actin filaments and not individual actin monomers in solution (Drees *et al.*, 2005). Both the shape and attachment angle of αE-catenin ABD density on actin filaments (Figure 2C) are similar to those of vinculin and its isoform metavinculin (Janssen *et al.*, 2006, 2012). The potential binding interface of the αE-catenin ABD (green "footprint" in Figure 2E) matched closely to that of vinculin, and, like vinculin, αE-catenin ABD binding did not alter actin filament symmetry (Janssen *et al.*, 2006).

Cooperative binding of αE-catenin ABD to filamentous actin can be inferred from the fact that filaments observed by cryo-EM have either no ABD bound at all or essentially all binding sites occupied (Figure 2A), despite the use of substoichiometric ABD concentrations. This arrangement can only occur if the ABD has a strong preference for binding in the vicinity of already bound ABDs. The

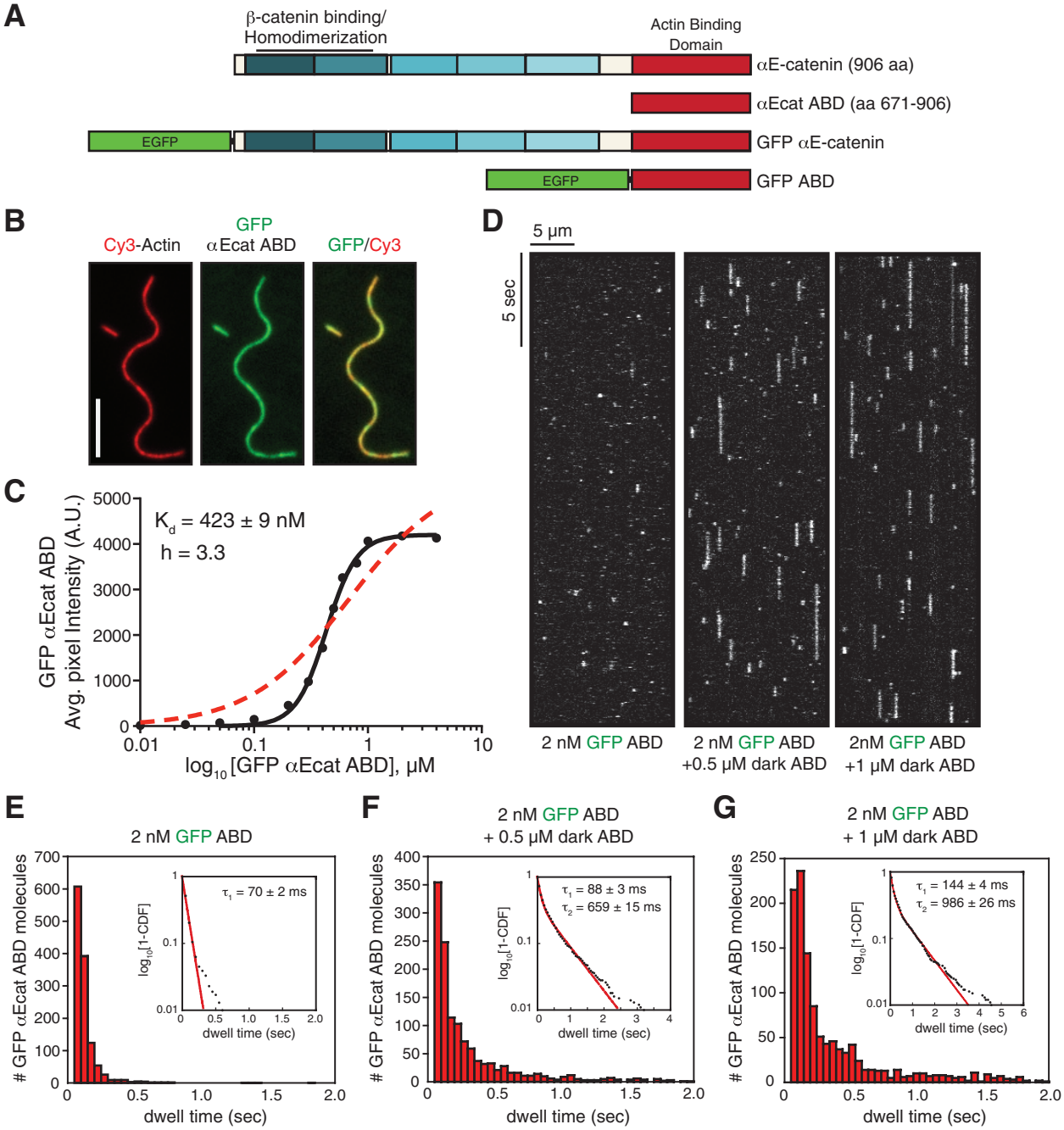

FIGURE 1: αE-catenin ABD binds cooperatively to actin filaments. (A) αE-catenin is composed of an array of five four-helix bundles (blue-shaded boxes) and a C-terminal five-helix bundle (red box). The β-catenin/homodimerization region and actin-binding domain are marked. All αE-catenin constructs used in this study are defined. (B) Localization of 1 μM GFP αE-catenin ABD bound to phalloidin-stabilized filamentous actin (20% Cy3 labeled). Scale bar, 5 μm. (C) Average fluorescence signal of GFP αE-catenin ABD bound to single-actin filaments plotted against total concentration of GFP αE-catenin ABD. Each data point represents average GFP fluorescence per pixel measured over ≥100 μm of single actin filaments (≥2 TIRF flow chambers). Data were fitted to either a Hill equation (black, straight line) or a hyperbolic function (red, dashed line). (D) Kymographs showing 2 nM GFP αE-catenin ABD binding and dissociating from the sides of single actin filaments in the absence or presence of 0.5 or 1 μM dark αE-catenin ABD. (E–G) Histograms of 2 nM GFP αE-catenin ABD dwell times on filamentous actin in the absence (E) or presence (F) of 0.5 μM dark αE-catenin ABD or (G) 1 μM dark αE-catenin ABD. Inset, curve fit of the 1-cumulative distribution frequency: (E) single-exponential fit (τ_1 = 70 ± 2 ms, n = 1244 molecules), (F) double-exponential fit (τ_1 = 88 ± 3 ms [58%]), τ_2 = 659 ± 15 ms [42%], n = 1289 molecules), and (G) double-exponential fit (τ_1 = 144 ± 4 ms [64%], τ_2 = 986 ± 26 ms [36%], n = 1210 molecules).

resolution of the current maps allows us to observe that binding of αE-catenin ABD is associated with a conformational change in the actin filament, including displacement of actin subdomain 2 away from the center of the filament (Figure 2D), which may contribute to cooperative αE-catenin ABD binding and affect other protein interactions (see later discussion).

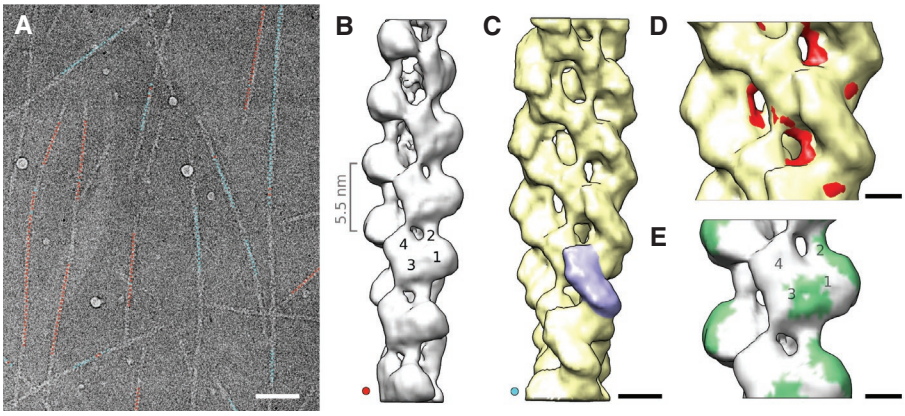

FIGURE 2: Cryo-EM and 3D reconstructions of actin filaments in the presence of αE-catenin ABD. (A) Representative electron micrograph of filamentous actin in the presence of αE-catenin ABD. The centers of segments used for reconstructions are marked in red (bare actin) and light blue (αE-catenin ABD decorated actin). The assignment was performed using a bias-free iterative sorting procedure (see *Materials and Methods*). Scale bar, 120 nm. (B) Reconstruction of bare actin filaments. Subdomains 1–4 are marked on one actin subunit. The distance between actin subunits along the long-pitch helix is indicated on the left. (C) Reconstruction of actin filaments with bound αE-catenin ABD. The extra density from a single αE-catenin ABD is highlighted in blue. Scale bar, 4 nm. (D) Overlay of decorated (C) and bare (B) actin filament reconstructions (differences in actin filament structure are marked in red) reveals that αE-catenin ABD binding induces a shift of actin subdomain 2 away from the filament center. Scale bar, 2 nm. (E) The "footprint" (green) of the extra density in the decorated filaments on the bare actin filament shows the potential binding surfaces of αE-catenin ABD. Scale bar, 2 nm.

Because binding of αE-catenin ABD to actin filaments is cooperative and affects actin protomer conformation, we examined whether αE-catenin ABD binding affected actin polymerization kinetics. In the presence of 4 μM profilin-actin or 2 μM monomeric actin, actin filaments nucleated spontaneously and elongated at an average rate of 16.5 and 16 subunits/s, respectively (Figure 3A and Supplemental Figure S2A). However, in the presence of increasing concentrations of GFP αE-catenin ABD, barbed-end elongation slowed significantly (Figure 3A and Supplemental Figure S2A). Barbed-end elongation was continuous within the optical limits of our observations, suggesting that slower growth was unlikely the result of intermittent pauses in growth (Figure 3, B and C, and Supplemental Figure S2B); a similar effect was observed with untagged (dark) αE-catenin ABD (Figure 3A). Because αE-catenin induces actin filament bundling (Rimm *et al.*, 1995; Drees *et al.*, 2005), we tested whether the elongation rate in filament bundles was affected by αE-catenin binding. The filament elongation rates in bundles generated by GFP αE-catenin ABD or αE-catenin ABD were even slower and largely insensitive to higher–ionic strength buffers (Figure 3, D and E, and Supplemental Figure S2, C and D). Together these results reveal that αE-catenin ABD binding to filamentous actin reduces the rate of actin polymerization, especially upon filament bundling.

αE-catenin may regulate actin polymerization and cell dynamics through the Arp2/3 complex (Drees *et al.*, 2005; Benjamin *et al.*, 2010; Sarpal *et al.*, 2012), but the mechanisms are unknown. We used TIRF-M to directly examine how αE-catenin binding to actin filaments regulates Arp2/3-dependent filament nucleation and filament branching. In the presence of 1 μM Mg-ATP-actin and the Arp2/3 complex–activating VCA domain from SCAR, the Arp2/3 complex generated new (daughter) filaments from the sides of preexisting (mother) filaments with a frequency of 0.13 branches/μm of mother filament (Figure 4, A and C). In the presence of ≥500 nM GFP αE-catenin ABD (Figure 4A) or ≥2 μM full-length GFP αE-catenin (Figure 4B and Supplemental Movies S3 and S4), the branching frequency induced by the Arp2/3 complex decreased up to 14-fold (Figure 4C). Strong inhibition of Arp2/3 filament nucleation was also observed in the presence of "dark" αE-catenin ABD or full-length αE-catenin (Figure 4C), further indicating that the GFP tag does not perturb αE-catenin actin filament side-binding activity in vitro. Thus αE-catenin binding to filaments directly inhibits the nucleation of branched actin filaments by the Arp2/3 complex.

Assembly of functional actin networks also requires proteins that catalyze filament disassembly such as the severing protein cofilin (Oser and Condeelis, 2009). Using preassembled Cy3-labeled ADP actin filaments, we visualized fluorescently labeled human cofilin binding and filament severing using TIRF-M. Significantly, αE-catenin ABD or full-length αE-catenin reduced cofilin binding and concomitant actin filament severing in a concentration-dependent manner (Figure 5, A and B, and Supplemental Movie S5).

We extended these in vitro studies to examine the distributions of αE-catenin, the Arp2/3 complex, and actin filaments during formation of nascent cell–cell contacts in Madin–Darby canine kidney (MDCK) epithelial cells using superresolution 3D-SIM. In single cells, the p34 subunit of the Arp2/3 complex was concentrated along the actin-rich leading edges of cells, whereas αE-catenin was distributed uniformly across membrane protrusions (Figure 6A). To remove the large cytoplasmic pool of αE-catenin (Benjamin *et al.*, 2010) that might obscure localization to the cytoskeleton, we gently extracted cells with a low concentration of Triton X-100 in the presence of phalloidin (to stabilize actin networks) before fixation (Cramer and Mitchison, 1995; Figure 6, B and E–H). After extraction, most of the αE-catenin in membrane protrusions was lost, whereas p34 was retained (Figure 6B, line scans in C and D). This indicates that αE-catenin was either weakly or not associated with the actin cytoskeleton, which is consistent with the rapid single-molecule binding kinetics observed for GFP αE-catenin binding to F-actin in vitro (Figure 1, D–G).

Colocalization of αE-catenin and actin filaments was observed at initial cell–cell contacts between p34-enriched membrane protrusions (Figure 6E). Within 4 h (Figure 6F) and through 24 h (Figure 6G) of cell–cell adhesion, αE-catenin was enriched with actin filaments along cell–cell contacts and was also observed as puncta on bundles of actin filaments parallel to, but distal from, the actin immediately at cell–cell contacts (Figure 6H). The Arp2/3 complex was also present along cell–cell contacts, although the amount was reduced relative to the amount at the leading edge of lamellipodia, and the distribution of Arp2/3 complex was different from that of αE-catenin (Figure 6, F and G). This was confirmed by directly measuring colocalization between F-actin, αE-catenin, and p34 signals along cell–cell contacts using Pearson's *r*. This analysis revealed similar degrees of colocalization between F-actin and αE-catenin, and between F-actin and p34, but little correlation between the distribution of αE-catenin and p34 (Figure 6I).

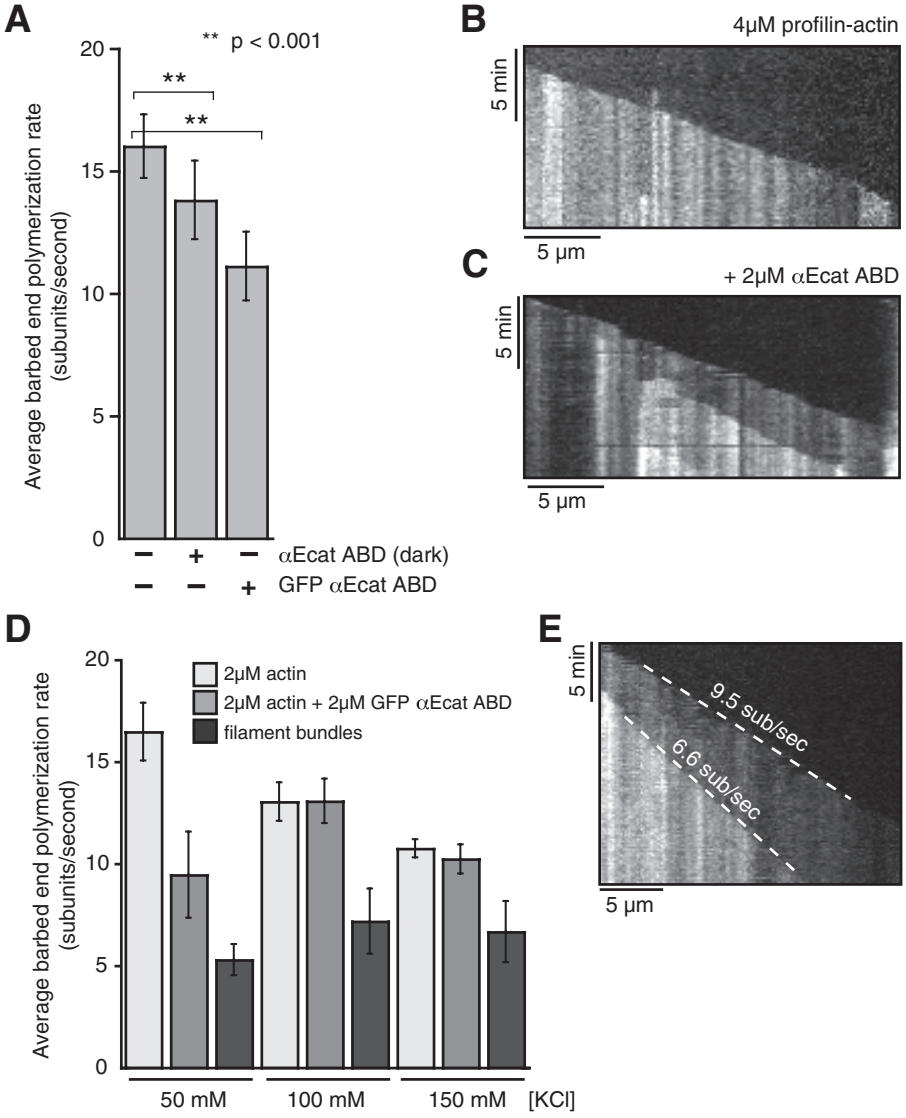

FIGURE 3: αE-catenin ABD reduces barbed-end elongation of filamentous actin. (A) Average barbed-end polymerization rates measured in the presence of 4 μM Mg-ATP-actin (5% Cy3 labeled) plus 4 μM human profilin 1. Copolymerization with either 2 μM GFP αE-catenin ABD or 2 μM αE-catenin ABD slows barbed-end elongation. The difference in single-actin-filament elongation rates in the presence of GFP αE-catenin ABD vs. dark αE-catenin ABD suggests that the GFP tag may interfere slightly with barbed-end elongation. Error bars, SD ($n \geq 30$ actin filaments from ≥2 experiments). (B, C) Representative kymographs of single actin filaments elongating in the presence of 4 μM Mg-ATP-Actin (5% Cy3 labeled) and 4 μM human profilin I alone (B) or in the presence of 2 μM αE-catenin ABD (C). (D) Barbed-end growth rates with 2 μM GFP αE-catenin ABD and increasing concentrations of KCl. Note that the barbed-end elongation in actin filament bundles is insensitive to the change in buffer ionic strength. (E) Kymograph showing bundling-dependent delay in barbed-end filament elongation in the presence of 2 μM Mg-ATP-actin, 2 μM GFP αE-catenin ABD, and 150 mM KCl. Dashed white lines mark the growing barbed ends of each filament in the kymograph.

DISCUSSION

Taken together, our results provide novel insights into the mechanism by which αE-catenin regulates actin network organization. αE-catenin binding to actin filaments reduces barbed-end polymerization, especially in the context of actin filament bundling, and also inhibits Arp2/3 complex–mediated branching and cofilin-mediated severing. Of note, αE-catenin ABD binding to actin filaments promotes a conformational change in the actin protomer that effects filament conformation. This may explain how αE-catenin binding inhibits filament branching by the Arp2/3 complex and severing by cofilin, since the Arp2/3 complex (Volkmann *et al.*, 2001; Rouiller *et al.*, 2008) and cofilin (Galkin *et al.*, 2011) contact or displace subdomain 2 of the actin protomer, which is structurally altered by αE-catenin ABD binding (Figure 2D). Thus αE-catenin may regulate Arp2/3 complex and cofilin binding to actin filaments by local steric interference at their binding site.

In addition to local structural changes, the cooperative nature of αE-catenin ABD binding (Figure 2) suggests that conformational changes in the actin filament away from the immediate site of ABD binding could further interfere with Arp2/3 and cofilin through an allosteric mechanism. This effect of αE-catenin may be similar to how cofilin promotes dissociation of the Arp2/3 complex from actin filaments by changing filament conformation (Chan *et al.*, 2009). The molecular nature of the observed cooperativity cannot be assessed at present due to the current resolution of the cryo-EM reconstructions. The twist of the actin filament does not change measurably, but the observed change in subdomain 2 might propagate along the long pitch of the helix by altering its interactions with a hydrophobic groove formed between subdomains 1 and 3 of a neighboring monomer. There may be additional, smaller changes in the other subdomains (i.e., small shifts in helix positions, minor rearrangements of loops, etc.) that contribute to propagated changes along this direction.

Our results provide a significant advance in understanding the interaction of αE-catenin with filamentous actin and, thereby, a mechanistic and structural framework for how αE-catenin binding to actin filaments may remodel the actin cytoskeleton during transitions between cell migration and cell–cell adhesion. An increased local concentration of αE-catenin associated with cadherin complexes clustering at cell–cell adhesions could change actin filament dynamics and organization locally by suppressing Arp2/3 complex–mediated branched actin organization in lamellipodia of migrating cells (Drees *et al.*, 2005; Benjamin *et al.*, 2010) and inducing the bundled organization of long, parallel actin filaments at cell–cell contacts (Hirokawa *et al.*, 1983). Indeed, analysis of αE-catenin in cells showed little correlation between the distributions of αE-catenin and the Arp2/3 complex (p34) along cell–cell contacts but colocalization of αE-catenin and bundles of actin filaments parallel to cell–cell contacts. These multiple biochemical activities may explain why loss of αE-catenin has such broad effects on cell behavior in development and disease.

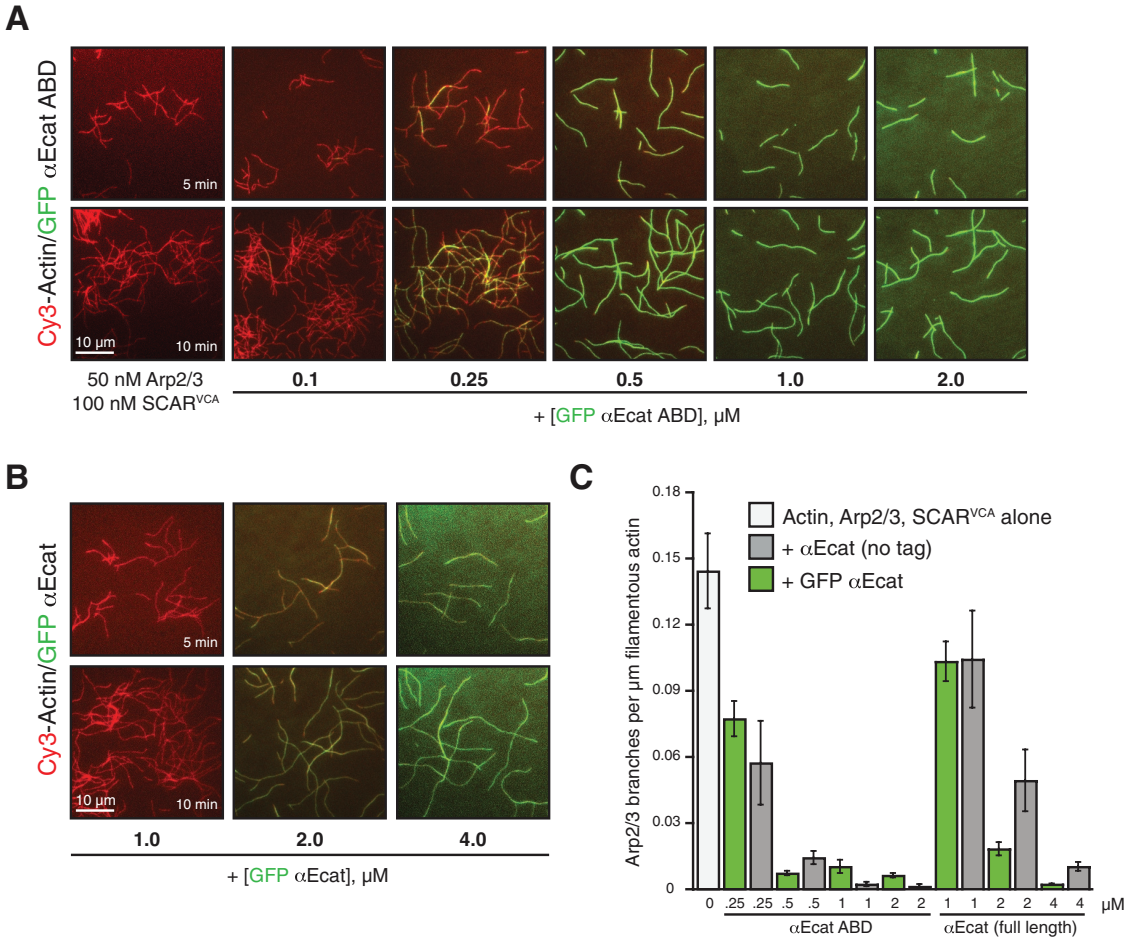

FIGURE 4: αE-catenin inhibits Arp2/3 complex branching of actin filaments. (A, B) Images of 1 μM Cy3-labeled Mg-ATP-actin polymerized with 50 nM Arp2/3 complex and 100 nM SCAR^{VCA} alone or in the presence of increasing concentrations of either GFP αE-catenin ABD (A) or full-length GFP αE-catenin (B). For each condition, all proteins were combined in TIRF buffer and flowed into the pegylated imaging chambers to initiate polymerization. The amount of spontaneous actin polymerization was not significantly affected by the presence of GFP αE-catenin. (C) Quantification of actin filament branching frequency. GFP αE-catenin ABD (A) and full-length GFP αE-catenin (green bars) are functionally equivalent to untagged αE-catenin proteins (gray bars). Error bars, SD (≥200 μm of filamentous actin from ≥2 experiments).

MATERIALS AND METHODS

Protein purification and labeling

Full-length murine αE-catenin (aa 1–906) and ABD (aa 671–906) were expressed as either N-terminal glutathione *S*-transferase (GST)-fusion proteins in pGEX-TEV or pGEX-4T, respectively, or as N-terminal histidine (His)-tagged enhanced GFP (EGFP) fusion proteins in pPROEX-HTa. Recombinant αE-catenin proteins were expressed in BL21 or BL21 (DE3) Codon Plus *Escherichia coli* cells (Pokutta and Weis, 2000). GST-tagged constructs bound to glutathione-agarose (Sigma-Aldrich, St. Louis, MO) were equilibrated in cleavage buffer (20 mM Tris, pH 8.0, 150 mM NaCl, 2 mM EDTA, 1 mM dithiothreitol [DTT], and 10% glycerol) and then incubated with TEV protease overnight at 4°C or bovine thrombin for 1 h at room temperature to cleave the GST tag. His-tagged proteins were purified on nickel-nitriloacetic acid agarose resin (Qiagen, Valencia, CA) and eluted with imidazole. Full-length αE-catenin proteins ("dark" and GFP tagged) were first loaded onto a Mono Q anion exchange column and eluted with ~200 mM NaCl. Eluted monomer protein was then further purified on a Superdex 200 gel filtration column (GE Healthcare) in 20 mM Tris, pH 8.0, 150 mM NaCl, 10% glycerol, and 1 mM DTT. ABD proteins were purified using a cation exchange Mono S column (GE Healthcare) and then by Superdex 200 gel filtration in 20 mM Tris, pH 8.0, 150 mM NaCl, 10% glycerol, and 1 mM DTT. Eluted protein was concentrated to 30–100 μM using a Millipore (Billerica, MA) column concentrator, flash frozen, and stored at 80°C. Note that the EGFP used in our experiments lacked the A206K mutation, which reduces dimerization (Zacharias *et al.*, 2002). Although EGFP can dimerize at high concentrations (EGFP dimer K_d = 110 μM), we found that the EGFP tag did not enhance or diminish the actin filament side-binding and actin filament–bundling activity of αE-catenin as judged by cosedimentation and the single–actin filament TIRF microscopy experiments.

Cytoplasmic actin was purified from *Acanthamoeba castellanii* (Gordon *et al.*, 1976; Zuchero, 2007). In brief, monomeric actin was stored at 4°C in 2 mM Tris, pH 8.0, 0.5 mM Tris(2-carboxyethyl)phosphine hydrochloride (TCEP), 0.1 mM $CaCl_2$, 0.2 mM ATP, and 0.01% azide and used within 3–6 mo. Monomeric actin was labeled on Cys-374 with Cy3-maleimide (GE Healthcare) on ice in the absence of reducing agent for 15 min. The reaction was quenched with 10 mM DTT and then centrifuged at 100,000 × *g* (TLA 100.4 rotor; Beckman Coulter, Brea, CA) to remove insoluble material. Labeled actin was then polymerized at room temperature by the addition of KMEI

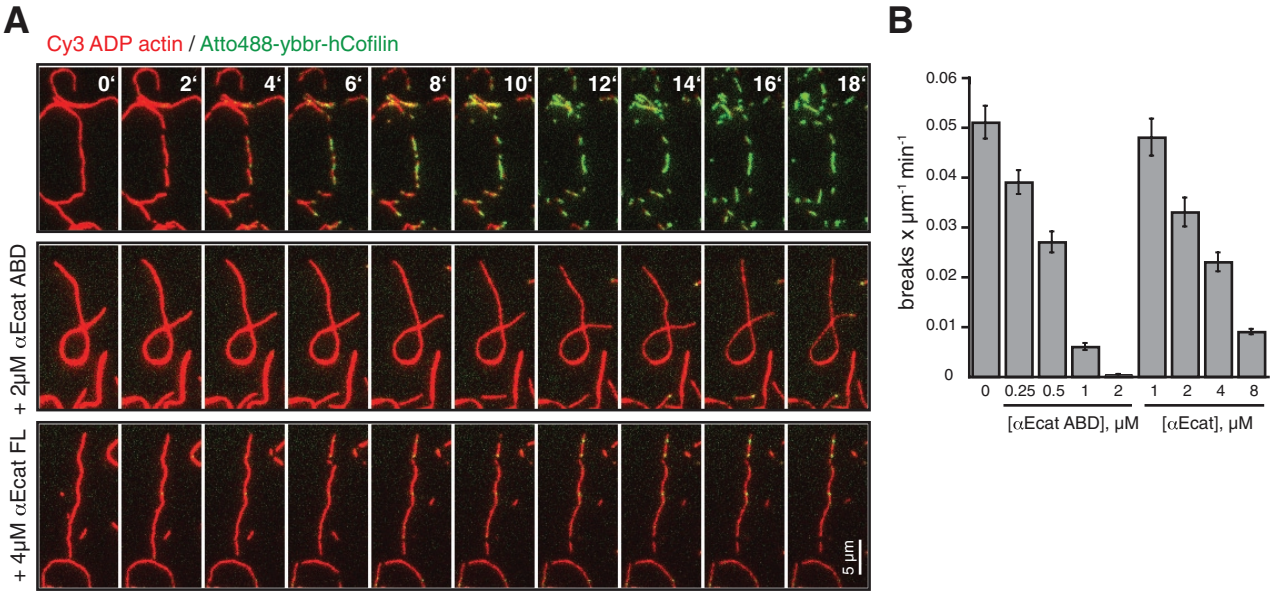

FIGURE 5: αE-catenin inhibits cofilin severing of actin filaments. (A) Montage of ADP actin filament (20% Cy3 labeled, red) disassembly in the presence of 75 nM Atto488-ybbr-hCofilin (green) alone or with αE-catenin ABD or full-length αE-catenin. Mixtures of Atto488-ybbr-hCofilin and αE-catenin (ABD and full-length protein) were flowed into the chamber simultaneously to initiate severing and actin filament binding, respectively. (B) Quantification of the cofilin-dependent actin filament severing rate (breaks μm^{-1} s^{-1}) in the presence or absence of αE-catenin ABD. Error bars, SD (≥200 μm of filamentous actin from ≥2 experiments).

buffer (50 mM KCl, 1 mM $MgCl_2$, 1 mM ethylene glycol tetraacetic acid [EGTA], 10 mM imidazole, pH 7.0) and 1 mM ATP. Polymerized actin was pelleted, washed with G-buffer (2 mM Tris, pH 8.0, 0.5 mM TCEP, 0.1 mM $CaCl_2$, 0.2 mM ATP, 0.01% azide), and resuspended in G-buffer to depolymerize filaments. After depolymerization in G-buffer for 5 d, actin was hard spun and gel filtered (Superdex 75; GE Healthcare). We typically achieved 40–60% labeling efficiency in the recovered material. The quality of labeled actin was determined by visualization of single-actin-filament elongation in vitro using TIRF-M.

Arp2/3 was purified as described (Dayel *et al.*, 2001). In brief, *A. castellanii* high-speed lysate was applied to a diethylaminoethane (DEAE) column (GE Healthcare). The DEAE flow through was then applied to an $NWASP^{VCA}$ column (NWASP covalently linked to a HiTrap NHS-activated HP column, 17-0717-01; GE Healthcare). After elution from the $NWASP^{VCA}$ column, Arp2/3 was further purified by cation exchange (Mono S) chromatography and gel filtration (Superdex 200).

Human cofilin I was cloned into a modified pETM-Z2 vector containing an N-terminal ybbR fusion (Z-Tag-his_{10}-TEV-ybbR-hCof1) and expressed in BL21 (DE3) Rosetta cells (EMD Millipore). We used a ybbR tag with the following peptide sequence: GDSLSWLLRLLN (Zhou *et al.*, 2007). After microfluidization of cells and ultracentrifugation, Z-Tag-his_{10}-TEV-ybbR-hCof1 containing bacterial lysate was batch bound to a 5-ml Hi-Trap Cobalt charged column. The eluate was cleaved with TEV protease to remove Z-Tag-his_{10}. Purification of ybbR-hCof1 was achieved by cation exchange (Mono S) and size exclusion (Superdex 200) chromatography. Pure ybbR-hCof1 was subsequently labeled in vitro using purified Sfp phosphopantetheinyl transferase and Atto488-CoA (S9348S; NEB, Ipswich, MA) as described (Yin *et al.*, 2005). Atto488-ybbR-hCof1 was functionally indistinguishable from human cofilin in our single-actin-filament TIRF assay, as well as in solution-based actin filament–severing assays.

Single-actin-filament TIRF assay

Counterglass slides (24 × 75 × 1 mm; 12-544-7; Thermo Fisher Scientific, Waltham, MA) were sonicated in 3 M NaOH, followed by washes with water and sonication in 100% ethanol. To minimize protein depletion effects, counterglass slides were coated with poly-L-lysine (PLL)–poly(ethylene glycol) (PEG) as described (Huang *et al.*, 2000). PLL-PEG was allowed to dry on the glass before rinsing off excess reagent with MilliQ water. PEG-functionalized coverslips (18 × 18 mm) were then attached to the PLL-PEG–coated counterglass slides with double-stick tape. To reduce nonspecific binding to the PEG, the functionalized imaging chamber was washed with 1× phosphate-buffered saline (PBS), pH 7.2, containing 1% Pluronic F-127 (P2443; Sigma-Aldrich) and 100 μg/ml κ-casein (C0406; Sigma-Aldrich). Glass was then washed with buffer containing 10 mM 4-(2-hydroxyethyl)-1-piperazineethanesulfonic acid (HEPES), pH 7.0, 2 mM TCEP, 200 mM KCl, and 1 mg/ml bovine serum albumin (BSA). Next 50 nM streptavidin (S00-01; Rockland Immunochemicals, Gilbertsville, PA) was flowed into the imaging chamber and incubated for 30 s. Finally, the flow chamber was incubated with 50 nM biotin-PEG_{11} heavy meromyosin (HMM; EZ-Link Maleimide-PEG11-Biotin, 21911; Thermo Fisher Scientific) for 30 s before washing out excess biotin-HMM.

The single-actin-filament TIRF assay was performed as described (Hansen and Mullins, 2010; Hansen *et al.*, 2013). In brief, actin polymerization reactions were initiated by combining 1 μl of 10× ME (2 mM EGTA, 0.5 mM $MgCl_2$) with 9 μl of 4.44 μM monomeric actin (5–10% Cy3 labeled) for 2 min at room temperature. The Mg-ATP-actin was then combined with TIRF buffer to reach a final buffer composition of 1 μM actin (5–10% Cy3 labeled), 10 mM imidazole, pH 7.0, 1 mM EGTA, 1 mM $MgCl_2$, 50–100 mM KCl, 0.2% methylcellulose (cP400, M0262; Sigma-Aldrich), 1 mg/ml BSA (A0281; Sigma-Aldrich), 20 mM β-mercaptoethanol (M6250; Sigma-Aldrich), 20 mM glucose, 0.2 mM ATP (26209; Sigma-Aldrich), 125 μg/ml glucose oxidase (22778.01; Biophoretics, Sparks, NV),

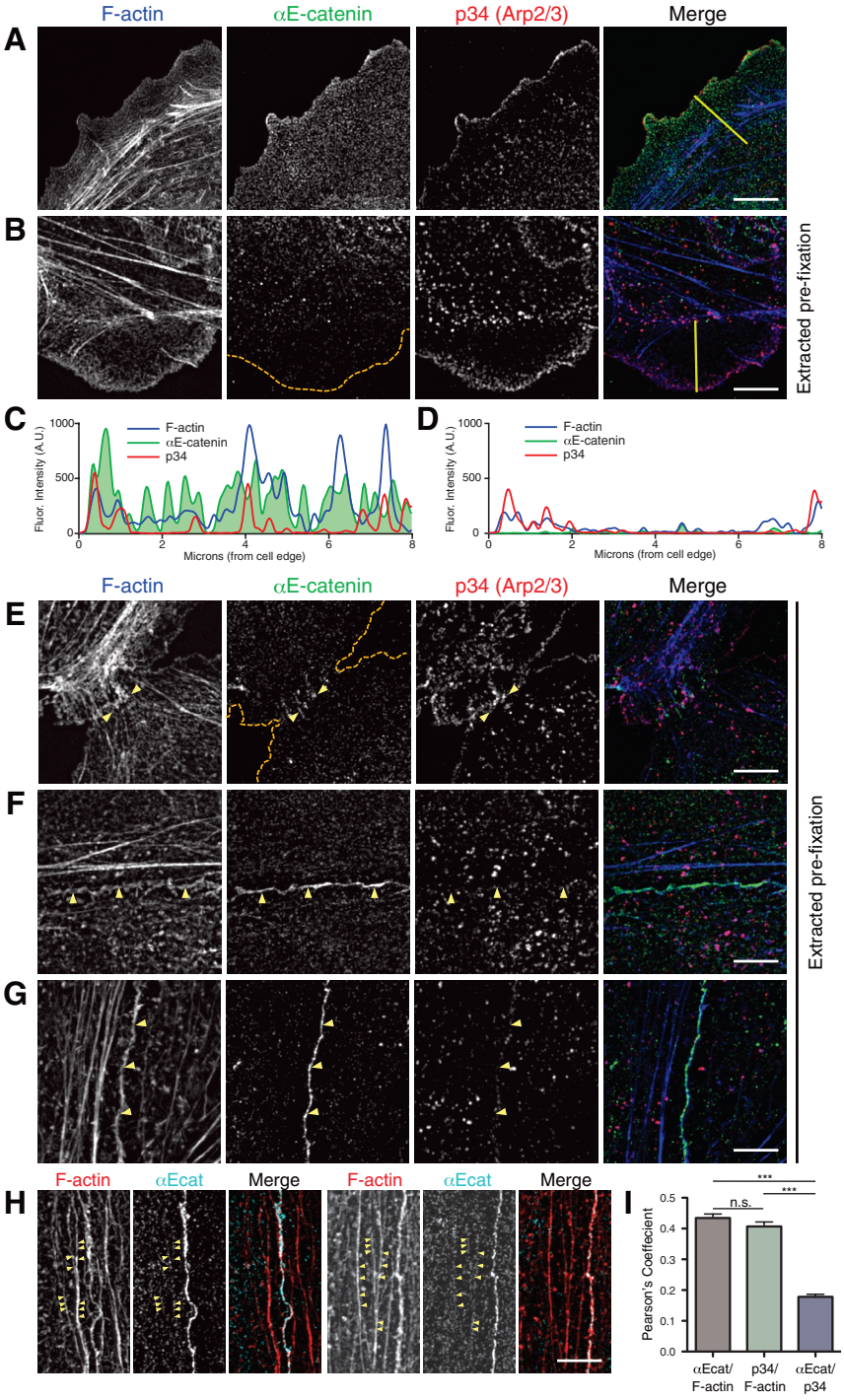

FIGURE 6: αE-catenin colocalizes with F-actin at developing cell–cell contacts. (A, B, E–H) 3D-SIM images of MDCK epithelial cells stained for F-actin, αE-catenin, and p34 (Arp2/3 complex). Scale bar, 5 μm. (A) Without extraction, αE-catenin is distributed throughout the cell and p34 is enriched along the leading edge. Yellow line marks line scan in C. (B) Preextraction decreases αE-catenin signal in membrane protrusions, whereas the p34 signal is retained. Orange dashed line marks the cell boundary; yellow line marks the line scan in D. (C, D) Representative line scans of F-actin, αE-catenin, and p34 signal intensities across the cell periphery in a control cell (C; yellow line in A) and a preextracted cell (D; yellow line in B). Preextraction removes the majority of the αE-catenin signal from the cell periphery, whereas the p34 signal is unperturbed. Note that the presence of unlabeled phalloidin during extraction reduces the intensity of the F-actin signal in preextracted cells relative to control cells. (E) At nascent contacts, p34 is abundant and αE-catenin is present. Orange dashed lines mark cell boundaries; yellow arrows indicate areas of αE-catenin accumulation along the contact. (F, G) At 4-h (F) and 24-h (G) cell–cell contacts, αE-catenin is enriched along the F-actin–rich adhesion, whereas p34 localization there is limited. Yellow arrows identify the cell–cell contact. (H) After preextraction, αE-catenin is occasionally observed along F-actin bundles, often adjacent to cell–cell contacts. Yellow arrows mark αE-catenin puncta along actin bundles. (I) Pearson's *r* was calculated between individual channels along cell–cell contacts. Both αE-catenin and p34 displayed similar levels of colocalization with F-actin; however, there was little correlation between αE-catenin and p34 signals (***$p < 0.0001$; one-way analysis of variance with Tukey's range test). Errors bars, SEM (35 images, >40 contacts measured).

and 20 μg/ml catalase (from bovine liver; C40-100MG; Sigma-Aldrich). The glucose oxidase and catalase solutions were made fresh from dry reagents, ultracentrifuged to remove debris (TLA120.1, 278,587 × *g*, 20 min), and used within 3 d.

For the cofilin-severing experiments, ADP-actin filaments were generated by polymerizing monomeric actin for at least 1 h in KMEI buffer (50 mM KCl, 1 mM $MgCl_2$, 1 mM EGTA, 10 mM imidazole, pH 7) lacking additional ATP or αE-catenin. The amount of time required for phosphate release after the rapid nucleotide hydrolysis is ~6 min (Melki *et al.*, 1996). ADP-actin filaments were then quickly diluted into buffer that contained 100 nM monomeric actin (critical concentration for actin-filament barbed-end growth). Actin filament was flowed into the imaging chamber using a wide-bore pipette tip to avoid sheering and captured by biotin-HMM–attached biotin-PEG/PEG surfaces coated with streptavidin. Unattached actin filaments were washed out of the imaging chamber. Finally, a mixture of 488-ybbr-cofilin and αE-catenin diluted in TIRF imaging buffer was flowed into the chamber to initiate filament severing. Actin filaments were visualized immediately.

To generate the GFP αE-catenin binding curve using TIRF-M (Figure 1), we first polymerized 2 μM monomeric actin (20% Cy3) for 1–2 h in KMEI buffer containing 2 μM dark phalloidin. Using wide-bore pipette tips, we diluted stabilized actin filaments into KMEI buffer to a concentration of 20 nM. Actin filaments were then flowed into the TIRF imaging chamber (silanized/pegylated and coated with streptavidin/biotin-HMM; see earlier description) and incubated for 1 min. Unbound actin filaments were washed out of the chamber with KMEI buffer. Finally, different concentrations of GFP αE-catenin were flowed into individual chambers. Images were acquired using the identical camera settings, laser power, and

filters for all concentrations of GFP αE-catenin added. We measured the average pixel intensity of fluorescent GFP αE-catenin attached to the sides of single actin filaments over >100 μm of actin filament length. We observed no difference in actin filament–binding activity for GFP αE-catenin in the presence or absence of phalloidin stabilization.

Fluorescence microscopy, software, and data analysis

All TIRF microscopy data were collected on a Nikon Eclipse TE2000-E (Nikon Instruments, Melville, NY) using Nikon Perfect focus at 25°C. All images were acquired with a cooled Andor iXon electron-multiplying charge-coupled device (EM CCD) camera (Andor Technologies, Belfast, United Kingdom) using Micromanager 3.0 software (Stuurman *et al*., 2007). Fluorescent dyes were excited through a 100× Apo Nikon TIRF objective (numerical aperture 1.49) using either a 491-nm (50 mW) or 561-nm (50 mW) laser.

Curve fitting for determination of the K_d of filamentous actin binding of GFP αE-catenin was solved using Prism software using a one-site specific binding model with Hill coefficient. Single molecule lifetime data for GFP αE-catenin were fitted to either a single exponential of $\log_{10}(1 - \text{CDF})$ [1*exp(–M_0/m_1)] or a double exponential of $\log_{10}(1 - \text{CDF})$ [m_2*exp(–M_0/m_1) + (1 – m_2)*exp(–M_0/m_3)] using KaleidaGraph software, where CDF = cumulative distribution frequency, M_0 = data value fit (i.e., time, x-axis value), m_1 = dwell time (τ_1), m_2 = fraction of molecules with τ_1 dwell time, m_3 = dwell time (τ_2). Variables m_1, m_2, and m_3 were floated when fitting the curve. Error bars for dwell times represent SEM from curve fitting. The statistical significance of the αE-catenin–dependent changes in single-actin-filament barbed-end polymerization rates was evaluated using an unpaired two-tail Student's *t* test in Excel (Microsoft, Redmond, WA). Final figures were generated using ImageJ (National Institutes of Health, Bethesda, MD), Photoshop (Adobe, San Jose, CA), and Illustrator (Adobe).

Electron cryo-microscopy and image analysis

Rabbit skeletal muscle actin was prepared and stored as described (Volkmann *et al*., 2000). Filamentous actin was used within 1–2 wk of preparation. Flash-frozen αE-catenin ABD was used within 1 wk of thawing. Both filamentous actin and αE-catenin ABD were diluted to 5 mM $NaPO_4$, pH 7.0, 60 mM NaCl, 1 mM $MgCl_2$, 0.1 mM EGTA, and 2 mM NaN_3. Actin filaments were diluted to 0.02 mg/ml, and αE-catenin ABD samples were diluted to 0.05 mg/ml. After 10 min of incubation, 4 μl from the final 1:2 (wt/wt) mixture was applied to ultraviolet glow discharged 400-mesh copper grids coated with Holey Triafol carbon film made in house. After 1 min of incubation in a humidified chamber, excess liquid was blotted, and the samples were plunge-frozen in liquid nitrogen–cooled liquefied ethane. Low-dose images were recorded with a Tecnai F20 (FEG) electron microscope (FEI Company, Hillsboro, OR) at a nominal magnification of 50,000 at 200 keV and 2.5-μm defocus (electron dose, 20 $e^-/Å^2$). The micrographs (Kodak Electron Image Film SO-163) were digitized with a SCAI scanner (Hexagon Geosystems, Madison, AL) with a pixel size of 0.3 nm on the sample. Two independent biochemical preparations of ABD αE-catenin were used.

Iterative reconstruction and sorting procedure

An iterative reconstruction/sorting protocol was used. For the reconstruction component, a modified protocol of the iterative helical real-space reconstruction method (Egelman, 2000) was used. This modification uses components from EMAN (Ludtke *et al*., 1999), SPARX (Hohn *et al*., 2007), and CoAn (Volkmann and Hanein, 1999) and was shown to give higher fidelity in the angle assignment step and allows backmapping of the segments included in the final reconstruction (Volkmann *et al*., 2005). The selected segments were 40 × 40 nm (~15 actin protomers) and spaced ~5.5 nm apart along the axis of filaments in the micrographs (Figure 2A). A total of 34,390 segments were selected from 33 micrographs after correction for the contrast transfer of the microscope (Mallick *et al*., 2005). For the initial sorting step, all selected segments were aligned along their helical axis; then, the intensities were projected down the helical axis for each segment, resulting in a one-dimensional intensity profile for each selected segment. Because a complete crossover of the filament is contained in each segment, the profiles are invariant of location along the filament. Furthermore, the averaging along the axis improves the signal-to-noise ratio dramatically. As a consequence, the profiles are highly sensitive to changes in filament width, that is, the presence or absence of bound material.

Once the intensity profiles were generated as described, a reference-free *K*-means clustering was used to classify the segments. The data segregated readily into two main groups with a significant difference in width. These two groups were then separately reconstructed using a cylindrical density as reference and the standard actin-filament symmetry parameters (rise, 2.75 nm; twist, −166.66°) as a starting point. To ensure absence of bias, perturbed symmetry values (rise, ±1, ±3) were also used as starting points, which converged to the same reconstructions/symmetry as those started with actual actin symmetry. The resulting reconstructions were already similar to those shown in Figure 2, with one resembling bare actin and the other showing clear extra densities. To improve resolution and correct for possible misclassifications from the intensity profiles, we used these initial reconstructions for reference-based sorting of the segments, iterating the process until convergence, that is, until no segments swapped classes (three rounds). Only 5% of the segments were reclassified from the original assignment, demonstrating the robustness and efficiency of the profile-based sorting procedure. The final classes contained 22,740 and 11,650 segments for the bare and decorated filaments, respectively. The resolution of the reconstructions (~1.8 nm) was determined with the 0.5 cutoff criterion of the Fourier shell correlation. Optimal alignment of the maps was achieved using CoAn (Volkmann and Hanein, 1999). The "footprint" of the bound ABD was determined by calculating a difference map between decorated and bare filaments from the aligned maps and then mapping the close contacts between the difference map and the bare filament reconstruction onto the bare filament reconstruction.

Glass silanization and pegylation

Glass was functionalized as described (Bieling *et al*., 2010), with modifications. In brief, coverglass (18 × 18 mm square; No. 1.5; Corning, Corning, NY) was cleaned by sonication in 3 M NaOH, followed by piranha etching (25% hydrogen peroxide, 75% sulfuric acid). After washing of the glass with MilliQ water, a coverslip sandwich was incubated with 100% GOPTS (3-glycidyloxypropyl trimethoxysilane) for 30 min at 75°C. Glass was then washed with anhydrous acetone (RT 10016; Electron Microscopy Sciences, Hatfield, PA) to remove excess silane. Next dry hydroxyl-$PEG_{3000\ Da}$-NH_2 (95%) and CH_3O-biotin-$PEG_{3000\ Da}$-NH_2 (5%) were combined using a mortar and pestle (10-3000-20 and 10-3000-25-20, respectively; Rapp Polymere, Tübingen, Germany). The dry 95/5 amino-PEG mixture was then melted onto clean, silanized coverslips (~8 mg total per coverslip sandwich) and baked for ≥8 h at 75°C in glass weigh jars (03-420-5C; Thermo Fischer Scientific). The glass was then washed with copious amounts of MilliQ water before spin drying and storage in a dust-free container at room temperature.

Actin cosedimentation assay

Chicken G-actin was incubated in polymerization buffer (20 mM HEPES, pH 7.5 or 8.0, or 20 mM Tris, pH 8.0, and 100 mM KCl, 2 mM $MgCl_2$, 0.5 mM ATP, and 1 mM EGTA) for 1 h at room temperature to polymerize filaments. αE-catenin was diluted to different concentrations in reaction buffer (20 mM HEPES, pH 7.5 or 8.0, or 20 mM Tris, pH 8.0, and 150 mM NaCl, 2 mM $MgCl_2$, 0.5 mM ATP, 1 mM EGTA, and 1 mM DTT) with and without 2 µM F-actin and incubated for 30 min at room temperature. Samples were centrifuged at 435,000 × *g* for 20 min in a TLA 120.1 rotor (Beckman Ultracentrifuge). Supernatant and pellet samples were diluted in Laemmli sample buffer, separated by SDS–PAGE, and stained with either Coomassie blue or SYRPO Ruby gel stain (Life Technologies, Carlsbad, CA). Gels were imaged on a LI-COR (LI-COR Biosciences, Lincoln, NE; Coomassie stain) or Typhoon (GE Healthcare; SYPRO stain) scanner, and protein bands were measured and quantified in ImageJ or LI-COR software. Binding data were processed with Prism software (GraphPad Software, La Jolla, CA).

Small-angle x-ray scattering data collection

Small-angle x-ray scattering data were collected on Beamline 4-2 at the Stanford Synchrotron Radiation Lightsource (Menlo Park, CA). Data were measured at 5, 2.5, 1, and 0.5 mg/ml using freshly purified αE-catenin ABD in 20 mM Tris, pH 8.0, 150 mM NaCl, 1 mM TCEP, and 2% glycerol. Samples were loaded into a 1.5-mm quartz capillary flow cell maintained at 20°C, and 10 × 1 s exposures were measured for each concentration. The raw scattering data were normalized to the incident beam intensity and buffer scattering subtracted. Individual scattering curves were visually inspected before averaging to ensure that radiation damage was minimal. The molecular mass was obtained from the intensity at zero scattering angle, *I*(0), using water as the calibration standard and assuming a protein partial specific volume of 0.7586 cm^3/g (Orthaber *et al.*, 2000). Crysol (Svergun *et al.*, 1995) was used to compute the radius of gyration, *Rg,* from the crystal structure of the vinculin ABD (Bakolitsa *et al.*, 1999).

Structured illumination microscopy

MDCK G type II epithelial cells were cultured in DMEM (1 g/l glucose; Life Technologies), 10% fetal bovine serum (Atlas Biologicals, Fort Collins, CO), and penicillin/streptomycin (Life Technologies). Cells were plated onto collagen-coated coverslips and fixed 4–24 h after plating in 4% paraformaldehyde (PFA) in PHEM buffer (60 mM 1,4-piperazinediethanesulfonic acid, pH 7.0, 25 mM HEPES, pH 7.0, 10 mM EGTA, pH 8.0, 2 mM $MgCl_2$, 0.12 M sucrose). For pre-fix extractions, cells were incubated for 20–30 s in PHEM buffer (without PFA) plus 0.1% Triton X-100 and 1 µg/ml unlabeled phalloidin before fixation in PFA/PHEM buffer (Cramer and Mitchison, 1995). After fixation, cells were washed with PBS, blocked overnight in PBS + 10% BSA at 4°C, washed in PBS, incubated with primary antibodies in PBS + 1% BSA for 1 h at room temperature (RT), washed three times in PBS, incubated with secondary antibodies and labeled phalloidin in PBS + 1% BSA for 1 h at RT, washed three times in PBS, and mounted in Fluoromount G (Electron Microscopy Sciences). The Arp2/3 complex was stained using anti–p34-Arc/ARPC2 (1:100, Millipore), αE-catenin was stained using anti–αE-catenin 15D9 (1:100; Enzo Life Sciences, Farmingdale, NY), and F-actin was stained using Alexa Fluor–labeled phalloidin (1:200–1:500; Life Technologies). Fixed cells were imaged on an N-SIM (Nikon Instruments) superresolution microscopy system with lateral (*x*, *y*) resolution of ~120 nm and axial (*z*) resolution of ~240 nm, nearly double that of a conventional optical microscope. Images were collected on an inverted Nikon ECLIPSE Ti-E equipped with a CFI Apo TIRF 100× oil (numerical aperture 1.49) objective and Andor Technology iXon DU897 EM CCD camera. The 3D-SIM image *Z*-stacks were processed and reconstructed in NIS Elements. Maximum projections of reconstructed image stacks were created for image analysis and presentation. Line scans (average pixel intensity along a 5 pixel–wide line) through membrane protrusions and signal colocalization (Pearson's *r*) at cell–cell contacts were measured using ImageJ.

ACKNOWLEDGMENTS

We thank Jim Bear (University of North Carolina, Chapel Hill, NC) for helpful comments on the manuscript. We are grateful to Thomas Weiss (Stanford Synchrotron Radiation Laboratory, Menlo Park, CA) for assistance with small-angle x-ray scattering measurements and Christina Goldbach and Adam Henry (Nikon Instruments) for assistance with SIM imaging. We also thank Peter Bieling (laboratory of Dyche Mullins, University of California, San Francisco) for purified and labeled Atto488-ybbr-cofilin. Small-angle x-ray scattering measurements were performed at the Stanford Synchrotron Lightsource, which is supported by the Department of Energy Office of Biological and Environmental Research and the National Institutes of Health. This work was supported by National Institutes of Health grants 1S10OD010625 (S.C.W.), GM035527 (W.J.N.), GM56169 (W.I.W.), 1U01GM094663 (W.J.N., W.I.W., N.V., D.H.), and GM61010 (R.D.M.); a March of Dimes Basil O'Connor Starter Scholar Research Award (A.V.K.); and a National Science Foundation Predoctoral Fellowship (S.D.H.).

REFERENCES

Aberle H, Butz S, Stappert J, Weissig H, Kemler R, Hoschuetzky H (1994). Assembly of the cadherin-catenin complex in vitro with recombinant proteins. J Cell Sci 107, 3655–3663.

Bakolitsa C, Cohen DM, Bankston LA, Bobkov AA, Cadwell GW, Jennings L, Critchley DR, Craig SW, Liddington RC (2004). Structural basis for vinculin activation at sites of cell adhesion. Nature 430, 583–586.

Bakolitsa C, de Pereda JM, Bagshaw CR, Critchley DR, Liddington RC (1999). Crystal structure of the vinculin tail suggests a pathway for activation. Cell 99, 603–613.

Benjamin JM, Kwiatkowski AV, Yang C, Korobova F, Pokutta S, Svitkina T, Weis WI, Nelson WJ (2010). AlphaE-catenin regulates actin dynamics independently of cadherin-mediated cell-cell adhesion. J Cell Biol 189, 339–352.

Benjamin JM, Nelson WJ (2008). Bench to bedside and back again: molecular mechanisms of alpha-catenin function and roles in tumorigenesis. Semin Cancer Biol 18, 53–64.

Bieling P, Telley IA, Hentrich C, Piehler J, Surrey T (2010). Fluorescence microscopy assays on chemically functionalized surfaces for quantitative imaging of microtubule, motor, and +TIP dynamics. Methods Cell Biol 95, 555–580.

Borgon RA, Vonrhein C, Bricogne G, Bois PR, Izard T (2004). Crystal structure of human vinculin. Structure 12, 1189–1197.

Chan C, Beltzner CC, Pollard TD (2009). Cofilin dissociates Arp2/3 complex and branches from actin filaments. Curr Biol 19, 537–545.

Choi HJ, Pokutta S, Cadwell GW, Bobkov AA, Bankston LA, Liddington RC, Weis WI (2012). alphaE-catenin is an autoinhibited molecule that coactivates vinculin. Proc Natl Acad Sci USA 109, 8576–8581.

Condeelis J, Singer RH, Segall JE (2005). The great escape: when cancer cells hijack the genes for chemotaxis and motility. Annu Rev Cell Dev Biol 21, 695–718.

Cramer LP, Mitchison TJ (1995). Myosin is involved in postmitotic cell spreading. J Cell Biol 131, 179–189.

Dayel MJ, Holleran EA, Mullins RD (2001). Arp2/3 complex requires hydrolyzable ATP for nucleation of new actin filaments. Proc Natl Acad Sci USA 98, 14871–14876.

Drees F, Pokutta S, Yamada S, Nelson WJ, Weis WI (2005). Alpha-catenin is a molecular switch that binds E-cadherin-beta-catenin and regulates actin-filament assembly. Cell 123, 903–915.

Egelman EH (2000). A robust algorithm for the reconstruction of helical filaments using single-particle methods. Ultramicroscopy 85, 225–234.

Galkin VE, Orlova A, Kudryashov DS, Solodukhin A, Reisler E, Schroder GF, Egelman EH (2011). Remodeling of actin filaments by ADF/cofilin proteins. Proc Natl Acad Sci USA 108, 20568–20572.
Gordon DJ, Eisenberg E, Korn ED (1976). Characterization of cytoplasmic actin isolated from *Acanthamoeba castellanii* by a new method. J Biol Chem 251, 4778–4786.
Halbleib JM, Nelson WJ (2006). Cadherins in development: cell adhesion, sorting, and tissue morphogenesis. Genes Dev 20, 3199–3214.
Hansen SD, Mullins RD (2010). VASP is a processive actin polymerase that requires monomeric actin for barbed end association. J Cell Biol 191, 571–584.
Hansen SD, Zuchero JB, Mullins RD (2013). Cytoplasmic actin: purification and single molecule assembly assays. Methods Mol Biol 1046, 145–170.
Hirokawa N 3rd, Keller TC, Chasan R, Mooseker MS (1983). Mechanism of brush border contractility studied by the quick-freeze, deep-etch method. J Cell Biol 96, 1325–1336.
Hohn M, Tang G, Goodyear G, Baldwin PR, Huang Z, Penczek PA, Yang C, Glaeser RM, Adams PD, Ludtke SJ (2007). SPARX, a new environment for cryo-EM image processing. J Struct Biol 157, 47–55.
Huang N-P, Michel R, Voros J, Textor M, Hofer R, Rossi A, Elbert DL, Hubbell JA, Spencer ND (2000). Poly(L-lysine)-g-poly(ethylene glycol) layers on metal oxide surfaces: surface-analytical characterization and resistance to serum and fibrinogen adsorption. Langmuir 17, 489–498.
Ishiyama N *et al*. (2013). An autoinhibited structure of alpha-catenin and its implications for vinculin recruitment to adherens junctions. J Biol Chem 288, 15913–15925 .
Izard T, Evans G, Borgon RA, Rush CL, Bricogne G, Bois PR (2004). Vinculin activation by talin through helical bundle conversion. Nature 427, 171–175.
Janssen ME, Kim E, Liu H, Fujimoto LM, Bobkov A, Volkmann N, Hanein D (2006). Three-dimensional structure of vinculin bound to actin filaments. Mol Cell 21, 271–281.
Janssen ME, Liu H, Volkmann N, Hanein D (2012). The C-terminal tail domain of metavinculin, vinculin's splice variant, severs actin filaments. J Cell Biol 197, 585–593.
Johnson RP, Craig SW (1994). An intramolecular association between the head and tail domains of vinculin modulates talin binding. J Biol Chem 269, 12611–12619.
Johnson RP, Craig SW (1995). F-actin binding site masked by the intramolecular association of vinculin head and tail domains. Nature 373, 261–264.
Kwiatkowski AV, Maiden SL, Pokutta S, Choi HJ, Benjamin JM, Lynch AM, Nelson WJ, Weis WI, Hardin J (2010). In vitro and in vivo reconstitution of the cadherin-catenin-actin complex from *Caenorhabditis elegans*. Proc Natl Acad Sci USA 107, 14591–14596.
Ludtke SJ, Baldwin PR, Chiu W (1999). EMAN: semiautomated software for high-resolution single-particle reconstructions. J Struct Biol 128, 82–97.
Mallick SP, Carragher B, Potter CS, Kriegman DJ (2005). ACE: automated CTF estimation. Ultramicroscopy 104, 8–29.
Melki R, Fievez S, Carlier MF (1996). Continuous monitoring of Pi release following nucleotide hydrolysis in actin or tubulin assembly using 2-amino-6-mercapto-7-methylpurine ribonucleoside and purine-nucleoside phosphorylase as an enzyme-linked assay. Biochemistry 35, 12038–12045.
Miller PW, Pokutta S, Ghosh A, Almo SC, Weis WI, Nelson WJ, Kwiatkowski AV (2013). *Danio rerio* alphaE-catenin is a monomeric F-actin binding protein with distinct properties from *Mus musculus* alphaE-catenin. J Biol Chem 288, 22324–22332.
Orthaber D, Bergmann A, Glatter O (2000). SAXS experiments on absolute scale with Kratky systems using water as a secondary standard. J Appl Crystallogr 33, 218–225.
Oser M, Condeelis J (2009). The cofilin activity cycle in lamellipodia and invadopodia. J Cell Biochem 108, 1252–1262.
Pokutta S, Drees F, Takai Y, Nelson WJ, Weis WI (2002). Biochemical and structural definition of the l-afadin- and actin-binding sites of alpha-catenin. J Biol Chem 277, 18868–18874.
Pokutta S, Weis WI (2000). Structure of the dimerization and beta-catenin-binding region of alpha-catenin. Mol Cell 5, 533–543.
Rangarajan ES, Izard T (2012). The cytoskeletal protein alpha-catenin unfurls upon binding to vinculin. J Biol Chem 287, 18492–18499.
Rangarajan ES, Izard T (2013). Dimer asymmetry defines alpha-catenin interactions. Nat Struct Mol Biol 20, 188–193.
Ratheesh A, Yap AS (2012). A bigger picture: classical cadherins and the dynamic actin cytoskeleton. Nat Rev. Mol Cell Biol 13, 673–679 .
Rimm DL, Koslov ER, Kebriaei P, Cianci CD, Morrow JS (1995). Alpha 1(E)-catenin is an actin-binding and -bundling protein mediating the attachment of F-actin to the membrane adhesion complex. Proc Natl Acad Sci USA 92, 8813–8817.
Rouiller I, Xu XP, Amann KJ, Egile C, Nickell S, Nicastro D, Li R, Pollard TD, Volkmann N, Hanein D (2008). The structural basis of actin filament branching by the Arp2/3 complex. J Cell Biol 180, 887–895.
Sarpal R *et al*. (2012). Mutational analysis supports a core role for Drosophila aE-catenin in adherens junction function. J Cell Sci 125, 233–245.
Stuurman N, Amoday N, Vale RD (2007). µManager: open source software for light microscopy imaging. Microsc Today 15, 42–43.
Svergun D, Barberato C, Koch MHJ (1995). CRYSOL—a program to evaluate x-ray solution scattering of biological macromolecules from atomic coordinates. J Appl Crystallogr 28, 768–773.
Svitkina TM, Borisy GG (1999). Arp2/3 complex and actin depolymerizing factor/cofilin in dendritic organization and treadmilling of actin filament array in lamellipodia. J Cell Biol 145, 1009–1026.
Vasioukhin V, Bauer C, Yin M, Fuchs E (2000). Directed actin polymerization is the driving force for epithelial cell-cell adhesion. Cell 100, 209–219.
Volkmann N, Amann KJ, Stoilova-McPhie S, Egile C, Winter DC, Hazelwood L, Heuser JE, Li R, Pollard TD, Hanein D (2001). Structure of Arp2/3 complex in its activated state and in actin filament branch junctions. Science 293, 2456–2459.
Volkmann N, Hanein D (1999). Quantitative fitting of atomic models into observed densities derived by electron microscopy. J Struct Biol 125, 176–184.
Volkmann N, Hanein D, Ouyang G, Trybus KM, DeRosier DJ, Lowey S (2000). Evidence for cleft closure in actomyosin upon ADP release. Nat Struct Biol 7, 1147–1155.
Volkmann N, Liu H, Hazelwood L, Krementsova EB, Lowey S, Trybus KM, Hanein D (2005). The structural basis of myosin V processive movement as revealed by electron cryomicroscopy. Mol Cell 19, 595–605.
Yang J, Dokurno P, Tonks NK, Barford D (2001). Crystal structure of the M-fragment of alpha-catenin: implications for modulation of cell adhesion. EMBO J 20, 3645–3656.
Yin J, Straight PD, McLoughlin SM, Zhou Z, Lin AJ, Golan DE, Kelleher NL, Kolter R, Walsh CT (2005). Genetically encoded short peptide tag for versatile protein labeling by Sfp phosphopantetheinyl transferase. Proc Natl Acad Sci USA 102, 15815–15820.
Zacharias DA, Violin JD, Newton AC, Tsien RY (2002). Partitioning of lipid-modified monomeric GFPs into membrane microdomains of live cells. Science 296, 913–916.
Zhou Z, Cironi P, Lin AJ, Xu Y, Hrvatin S, Golan DE, Silver PA, Walsh CT, Yin J (2007). Genetically encoded short peptide tags for orthogonal protein labeling by Sfp and AcpS phosphopantetheinyl transferases. ACS Chem Biol 2, 337–346.
Zuchero JB (2007). In vitro actin assembly assays and purification from *Acanthamoeba*. Methods Mol Biol 370, 213–226.